Int. J. Radiation Oncology Biol. Phys., Vol. 81, No. 3, pp. 871–879, 2011

0360-3016/$ - see front matter

ELSEVIER

doi:10.1016/j.ijrobp.2010.11.078

PHYSICS CONTRIBUTION

ACCURATE ANALYSIS OF THE CHANGE IN VOLUME, LOCATION, AND SHAPE OF METASTATIC CERVICAL LYMPH NODES DURING RADIOTHERAPY

SEISHIN TAKAO, PH.D.,* SHIGERU TADANO, PH.D.,* HIROSHI TAGUCHI, M.D., PH.D.,† KOICHI YASUDA, M.D.,† RIKIYA ONIMARU, M.D., PH.D.,† MASAYORI ISHIKAWA, PH.D.,‡ GERARD BENGUA, PH.D.,‡ RYUSUKE SUZUKI, PH.D.,‡ AND HIROKI SHIRATO, M.D., PH.D.†

*Graduate School of Engineering, †Graduate School of Medicine, and ‡Department of Medical Physics, Hokkaido University, Sapporo, Japan

Purpose: To establish a method for the accurate acquisition and analysis of the variations in tumor volume, location, and three-dimensional (3D) shape of tumors during radiotherapy in the era of image-guided radiotherapy.
Methods and Materials: Finite element models of lymph nodes were developed based on computed tomography (CT) images taken before the start of treatment and every week during the treatment period. A surface geometry map with a volumetric scale was adopted and used for the analysis. Six metastatic cervical lymph nodes, 3.5 to 55.1 cm^3 before treatment, in 6 patients with head and neck carcinomas were analyzed in this study. Three fiducial markers implanted in mouthpieces were used for the fusion of CT images. Changes in the location of the lymph nodes were measured on the basis of these fiducial markers.
Results: The surface geometry maps showed convex regions in red and concave regions in blue to ensure that the characteristics of the 3D tumor geometries are simply understood visually. After the irradiation of 66 to 70 Gy in 2 Gy daily doses, the patterns of the colors had not changed significantly, and the maps before and during treatment were strongly correlated (average correlation coefficient was 0.808), suggesting that the tumors shrank uniformly, maintaining the original characteristics of the shapes in all 6 patients. The movement of the gravitational center of the lymph nodes during the treatment period was everywhere less than ±5 mm except in 1 patient, in whom the change reached nearly 10 mm.
Conclusions: The surface geometry map was useful for an accurate evaluation of the changes in volume and 3D shapes of metastatic lymph nodes. The fusion of the initial and follow-up CT images based on fiducial markers enabled an analysis of changes in the location of the targets. Metastatic cervical lymph nodes in patients were suggested to decrease in size without significant changes in the 3D shape during radiotherapy. The movements of the gravitational center of the lymph nodes were almost all less than ±5 mm. © 2011 Elsevier Inc.

Adaptive radiotherapy, Tumor deformation, Tumor geometry, Image-guided radiotherapy, Intensity-modulated radiation therapy.

INTRODUCTION

The latest advances in high-precision radiotherapy enable focusing of higher radiation doses to the tumor region while minimizing unwanted radiation exposure to surrounding tissue. Intensity-modulated radiation therapy (IMRT) varies the intensities and profiles of beams from various directions to fit the tumor size and shape. An initial treatment plan prescribing the radiation field and dose in IMRT is made based on information about the tumor location and geometry before treatment starts. If the tumor moves or shrinks during treatment, the surrounding normal tissue may become included in the region exposed to high radiation doses (1). Such potential anatomic changes can be measured and corrected during fractionated radiotherapy by any of several imaging techniques. Image-guided radiotherapy (IGRT) is one such technique for margin reduction caused by setup uncertainties or anatomic movement used to improve the accuracy of dose delivery. Many studies have reported interfractional organ motions and targeting errors in IGRT using daily computed tomography (CT) images (2–4). The clinical efficacy of IGRT techniques in reducing the treatment margins have been confirmed in head-and-neck cancer (5–7) and prostate cancer (8–10).

However, it is still not practical to perform daily modifications to treatment plans to adapt to observed changes in

Reprint requests to: Seishin Takao, Ph.D., Division of Human Mechanical Systems and Design, Graduate School of Engineering, Hokkaido University, N13 W8, Kita-ku, Sapporo, 060-8628, Japan. Tel: (+81) 11-706-6406; Fax: (+81) 11-706-6406; E-mail: takao@mech-me.eng.hokudai.ac.jp

Supported in part by a Grant-in-Aid for Scientific Research (A), MEXT (NO. 18209039) and Grant-in-Aid for JSPS Fellows (NO. 09J02587).

Conflict of interest: none.

Received March 25, 2010, and in revised form Oct 21, 2010. Accepted for publication Nov 29, 2010.

Table 1. Characteristics of the patients

Characteristic	Patient 1	2	3	4	5	6
Sex	F	M	F	M	M	M
TMN classification	T2bN2M0	T3N2M0	T3N2M0	T2bN1M0	T3N2M0	T1N1M0
Pathologic type						
Undifferentiated carcinoma /Squamous cell carcinoma	Undiff	Undiff	SqCC	Undiff	SqCC	Undiff
Treatment						
IMRT/Conventional RT (Conv)	IMRT	Conv	IMRT	IMRT	IMRT	IMRT
Dose (Gy)						
Total dose and number of fractions (fr)	66 (33 fr)	70 (35 fr)	70 (35 fr)	70 (35 fr)	70 (35 fr)	66 (33 fr)
Initial tumor volume (cm^3)	3.5	55.1	10.4	7.6	7.2	12.7

Abbreviations: Undiff = undifferentiated carcinoma; SqCC = squamous cell carcinoma; IMRT = intensity-modulated radiation therapy; RT = radiation therapy; Conv = conventional; fr = fractions.

the tumor dimensions. Several practical ways to minimize anatomic uncertainties have been reported. Hansen *et al.* proposed a strategy of repeated CT imaging and replanning to ensure adequate doses to the target volumes and safe doses to normal tissue during the course of IMRT (11). Smyth *et al.* verified the dose coverage in clinical target volumes at the time of treatment delivery using a dose distribution overlay technique (12). Several image registration methods have also been proposed for online replanning in IGRT (13–16). To improve the efficacy of practical solutions, accumulation of precise knowledge about the changes in tumor volumes, locations, and especially the three-dimensional (3D) shape during radiotherapy is critically important. The authors have proposed a method to

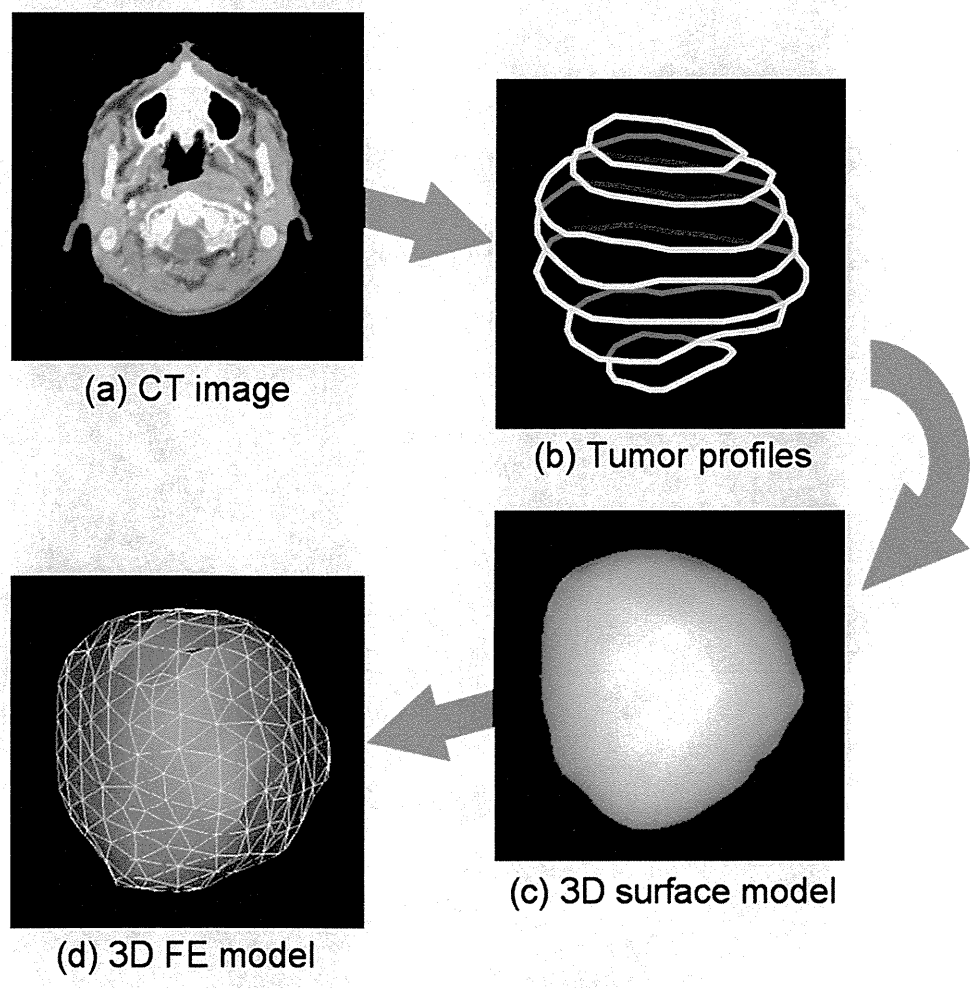

Fig. 1. Finite element modeling process for the tumors. (a) CT image for treatment planning. (b) Tumor contours on each slice. (c) 3D surface model of the tumor. (d) Finite element (FE) model of the tumor.

represent 3D tumor shapes in a two-dimensional (2D) map and evaluate the therapeutic response to radiotherapy (17).

The purpose of this study was to establish an accurate method for the acquisition and analysis of variations in tumor volumes, locations, and 3D shapes during radiotherapy. The 3D tumor geometry was expressed in terms of distances from the tumor center to the tumor boundary. This information is represented in 2D color-scaled maps of the distances from the center, from which the 3D tumor shapes can be visually and quantitatively assessed. Further, by comparison of maps before and after treatment, the therapeutic response can be evaluated quantitatively based on the changes in tumor shape during the course of treatments.

METHODS AND MATERIALS

Clinical cases

The study participants were 6 patients with nasopharyngeal cancer and metastatic cervical lymph nodes who were treated at the Hokkaido University Hospital, Sapporo, Japan, between February 2007 and November 2008. The patient characteristics are given in Table 1. Of the 6 patients, 3 had Stage T3N2M0 disease, and 3 patients were diagnosed with Stages T2bN2M0, T2bN1M0, and T1N1M0 disease, respectively. Four tumors were undifferentiated carcinomas and two were squamous cell carcinomas. The average target volume was 16.1 cm^3 (range, 3.5–55.2 cm^3). All the patients except the patient with the largest lymph node (Patient 2) were treated with IMRT; Patient 2 received conventional radiotherapy. The dose distribution before radiotherapy intended each node in this study to be homogeneously irradiated with a dose of 66 to 70 Gy in 2 Gy fractions delivered five times a week.

Pretreatment CT images (CT0) were taken for the treatment planning. The slice thickness of the pretreatment CT images was 2 mm. After the start of treatment, follow-up CT images were taken at weekly intervals (CT1, CT2, CT3, etc). The slice thickness of the follow-up CT images was 5 mm. All patients were immobilized by thermoplastic masks during the CT scanning and treatment. Additionally, in the head-and-neck IMRT treatments in our hospital, a mouthpiece with three fiducial markers (2-mm diameter gold pellets) was used in the fluoroscopic verification of the patient setup (18). This study was conducted with written informed consent

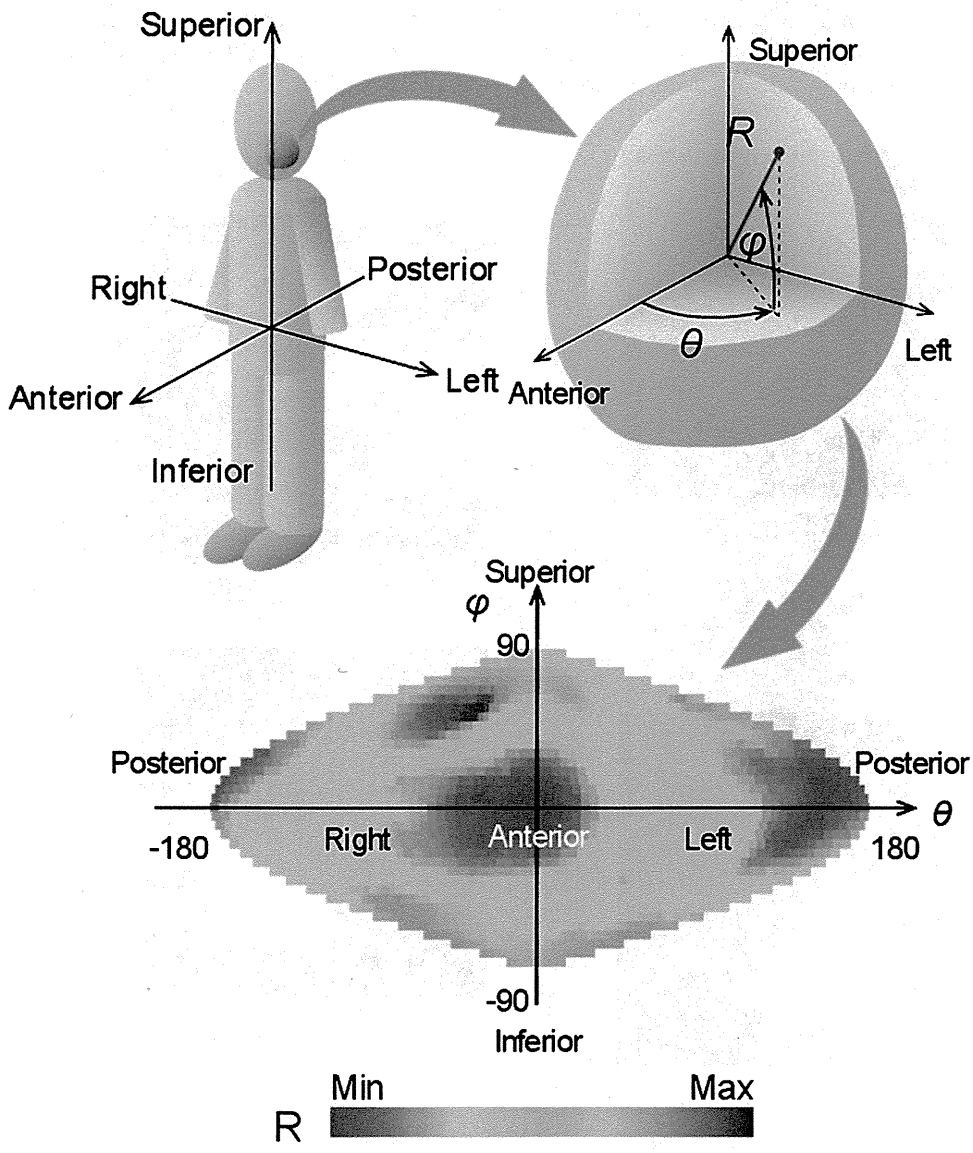

Fig. 2. Representation of the three-dimensional tumor geometry in a two-dimensional color map (surface geometry map).

obtained from all patients and was approved by the institutional ethical committee at Hokkaido University Hospital.

Finite element models of metastatic lymph nodes

Finite element (FE) models of the targets were constructed based on the tumor images. The procedure is shown in Fig. 1. One radiation oncologist (H. T.) determined and contoured metastatic cervical lymph nodes on the CT images with appropriate window settings by means of a radiotherapy planning system (Xio, Computerized Medical Systems, St. Louis, MO) (Fig. 1a). A group of sequential cross-sectional profiles of the tumor were then loaded into biomedical imaging software (Analyze PC 7.0, Mayo Foundation, Rochester, MN) and interpolated to 1-mm intervals (Fig. 1b). From these images, 3D surface models of the tumors were constructed and saved in DXF (Drawing Exchange Format) (Fig. 1c), and the DXF files were converted to IGES (Initial Graphics Exchange Specification) files. Finally, the IGES files were imported into the finite element analysis software package (ANSYS 11.0, ANSYS, Canonsburg, PA), and then the 3D FE models of the tumors were constructed (Fig. 1d).

Evaluation of tumor geometry and location

The quantitative evaluation of the 3D tumor geometry was performed using the distances from the tumor center to its surface at every angle (17). The values of the distances were represented by the radius R in a spherical coordinate system O-$R\theta\varphi$, with the origin set at the center of gravity of the tumor. The angle θ represents the azimuthal angle ($-180° \leq \theta \leq 180°$) with $\theta = 0°$ being the anterior plane. The positive rotation angle is counterclockwise around the origin. The angle φ represents the polar angle ($90° \leq \varphi \leq 90°$), and $\varphi = 0°$ is defined to be the horizontal plane. The distance from the origin to the tumor surface at (θ, φ) is expressed by the radius $R(\theta, \varphi)$, and radius $R(\theta, \varphi)$ was sampled at 10° intervals in both the polar and the azimuthal directions, giving a total of 684 sampling points. The 3D tumor geometry can be evaluated with the values of $R(\theta, \varphi)$. To enable a visual understanding of the features of the 3D geometry, a 2D surface geometry map like a global map is introduced (Fig. 2). In this map, the values of the tumor radius $R(\theta, \varphi)$ are represented in a color scale and plotted in the θ-φ plane: red indicates the maximum radius and blue the minimum within the tumor. The warm colors (red and yellow) represent convex areas, and cool colors (blue) represent concave areas. If the tumor is a perfect sphere, the map will be uniformly colored (green). This map is termed a surface geometry map. The size of the map was modified to express the tumor volume relative to the pretreatment tumor volume. For example, if the tumor volume decreases to half, the length of each side of the map becomes $(1/2)^{1/3}$.

The patterns of the surface geometry map represent morphologic features of the tumors, and it is possible to know whether the tumor shrinks uniformly by visually comparing maps based on the CT images acquired before and during treatment. Further, to evaluate changes in tumor geometry mathematically, the image correlation between the maps was analyzed. These surface geometry maps were converted into a grayscale with 256 levels; therefore, the intensities of the maps represent the tumor radius and were used in the correlational analysis of the images. The intensities at every position in the map during treatment were compared with those of the corresponding position in the map before treatment, and a correlation coefficient for these two maps was calculated. This image correlation coefficient indicates the similarity of two images, and where the two images are strongly correlated, it suggests that the tumor shrank uniformly.

The changes in tumor location were analyzed as the displacement of the gravitational center of a tumor. To examine the tumor movement during the treatment period, the coordinate systems of the weekly CT scans were translated and rotated so that they corresponded to the pretreatment CT scan using a CT–CT fusion technique. In the 5 patients treated with IMRT, the follow-up and pretreatment CT images were aligned with the reference images by means of the three fiducial markers implanted in the mouthpieces. The accuracy of the patient setup localization using the fiducial markers in the mouthpieces has been reported elsewhere (18). In the patient for whom the mouthpiece was not used, two images were matched based on the bone structure. The displacement of the gravitational center of a tumor was measured in the coordinate system of the pretreatment CT.

RESULTS

Details of changes in tumor volumes during the radiotherapy are shown in Table 2. After irradiation with 66 to 70 Gy, the tumor volumes decreased to 0.31 to 8.4 cm^3 (to 8.7–39 % of the initial volumes). In some cases, the measured tumor

Table 2. Tumor volume changes during treatment. Values in brackets under the sizes of the tumors show the number of days elapsed from start of treatment (negative values are days before start of treatment)

	Absolute (cm^3) and relative (%) tumor volume							
Patient	CT0	CT1	CT2	CT3	CT4	CT5	CT6	CT7
1	3.5 (100%)	2.2 (63%)	1.5 (44%)	1.1 (31%)	0.72 (20%)	0.56 (16%)	0.55 (15%)	0.31 (8.7%)
	(Day −20)	(Day 12)	(Day 19)	(Day 26)	(Day 33)	(Day 40)	(Day 48)	(Day 54)
2	55.1 (100%)	36.5 (66%)	19.1 (35%)	15.9 (29%)	14.3 (26%)	8.4 (15%)		
	(Day -6)	(Day 9)	(Day 19)	(Day 30)	(Day 34)	(Day 44)		
3	10.4 (100%)	9.5 (91%)	5.3 (51%)	4.1 (39%)	2.8 (27%)	2.5 (24%)	2.2 (21%)	2.4 (23%)
	(Day −21)	(Day 9)	(Day 15)	(Day 22)	(Day 29)	(Day 36)	(Day 43)	(Day 50)
4	7.6 (100%)	7.6 (101%)	4.1 (55%)	3.7 (48%)	3.4 (45%)	3.1 (41%)	2.1 (28%)	1.5 (20%)
	(Day −19)	(Day 7)	(Day 14)	(Day 21)	(Day 28)	(Day 35)	(Day 42)	(Day 49)
5	7.2 (100%)	9.5 (131%)	8.3 (115%)	6.6 (91%)	5.8 (80%)	4.0 (55%)	2.8 (39%)	
	(Day −13)	(Day 7)	(Day 14)	(Day 21)	(Day 27)	(Day 42)	(Day 49)	
6	12.7 (100%)	14.2 (112%)	8.0 (63%)	5.3 (42%)	4.1 (32%)	2.9 (23%)	2.5 (19%)	2.4 (15%)
	(Day −27)	(Day 9)	(Day 16)	(Day 23)	(Day 30)	(Day 37)	(Day 44)	(Day 51)

Abbreviations: CT0 = pretreatment computed tomography images; CT1 = CT images at 1 week; CT2 = CT images at 2 weeks, etc.

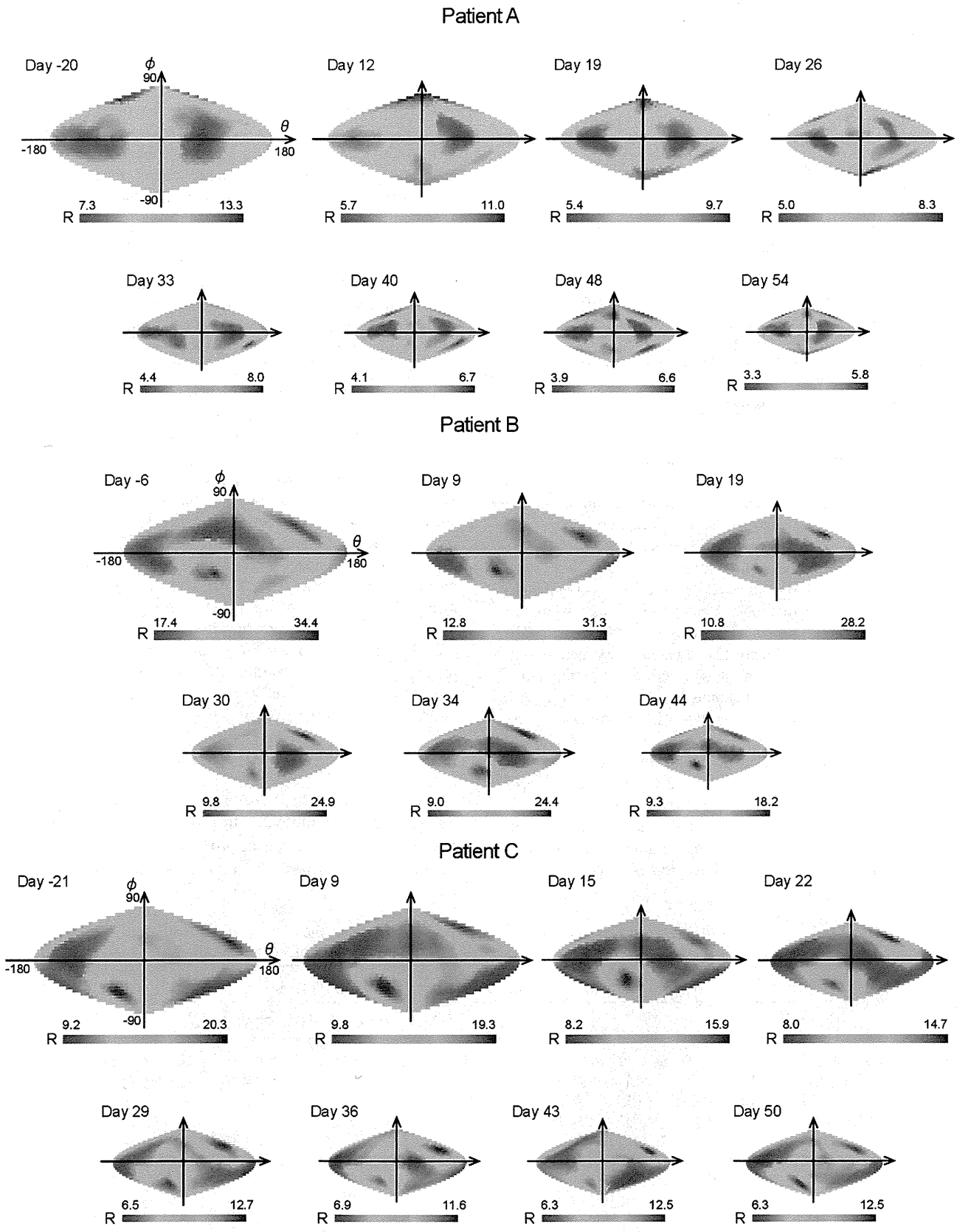

Fig. 3. Changes in three-dimensional tumor geometries during radiotherapy represented using surface geometry maps. Day + number represents the day of the CT examination after the starting date of radiotherapy for patients 1, 2, 3, 4, 5, and 6, respectively. Negative values are days before the start of treatment.

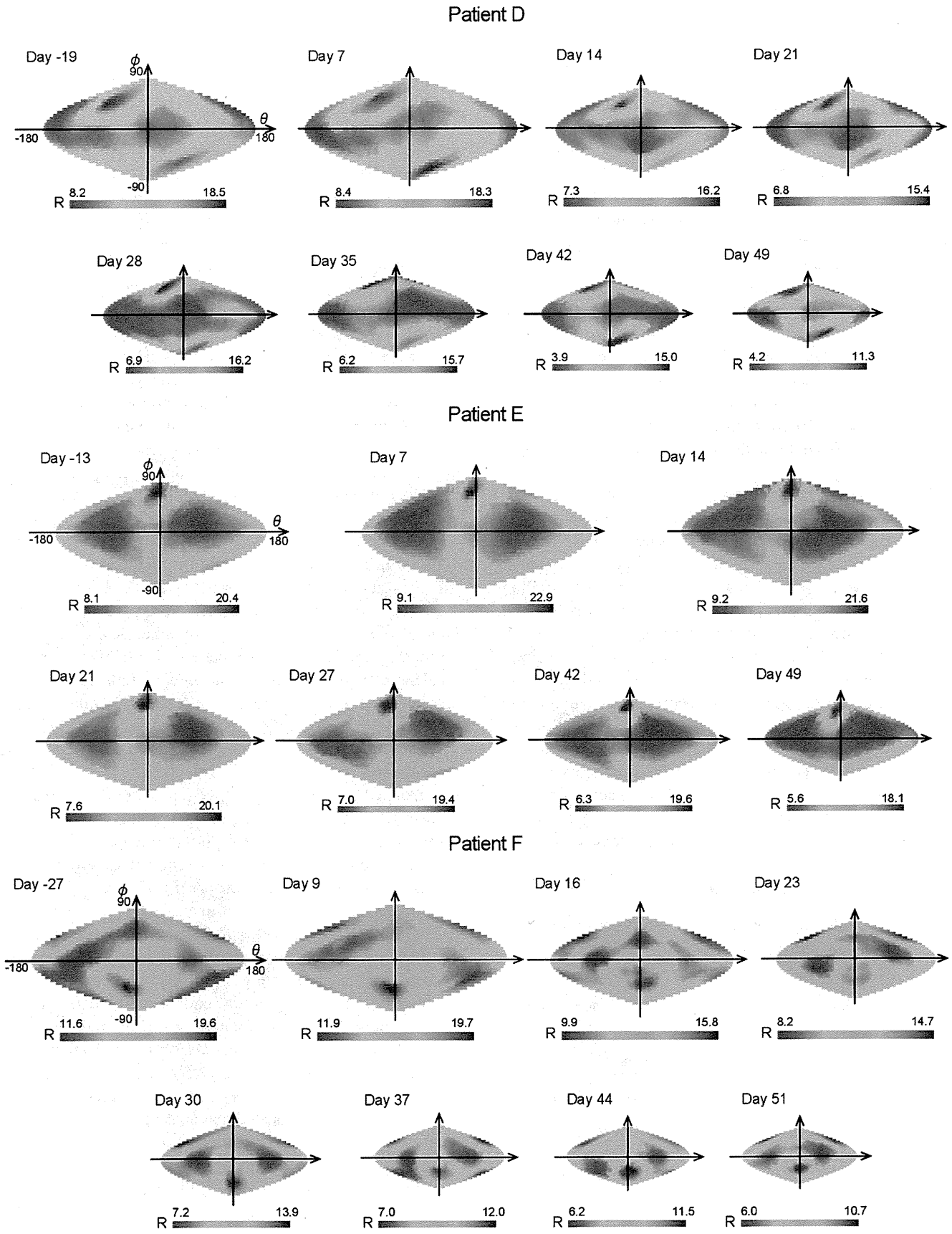

Fig. 3. (*continued*).

volumes at CT1 were larger than those at CT0, suggesting that tumor volumes increased during treatment planning. Changes in the tumor geometry during treatment are shown in Fig. 3 with the surface geometry maps. These maps show convex regions in red and concave regions in blue, allowing a visual understanding of the 3D tumor geometries. There are apparent differences in the distribution of red regions among the 6 patients before radiotherapy, showing that the deformation maps characterize the 3D shape of the tumors. In all 6 patients, the patterns of the colors did not change significantly during the treatment period even though the sizes of the tumors decreased dramatically. These results show that the six metastatic cervical lymph nodes shrank more or less evenly, maintaining the original characteristics of the 3D shape during the radiotherapy. Table 3 shows the image correlation coefficients between surface geometry maps constructed based on the CT images acquired before and during treatment. In all 6 patients, the maps obtained during treatment were strongly correlated statistically with the maps obtained before treatment; the average of the correlation coefficients in the six cases was 0.808 (range, 0.719–0.915).

Figure 4 shows the trajectories of the gravitational center of the tumors during treatment. Generally, the values of the displacement of the tumor centers were less than ±5 mm. In Patient 2, with the largest tumor volume before treatment and treated with conventional radiotherapy, the variation reached nearly 10 mm. Details of the tumor displacement during radiotherapy are shown in Table 4. The average displacement was 2.2 mm in the anterior–posterior (A–P) direction, 1.3 mm in the left–right (L–R) direction, and 2.2 mm in the superior–inferior (S–I) direction. The maximum displacement was 9.3 mm in the A–P direction (Patient 2), 4.1 mm in the L–R direction (Patients 2 and 4), and 9.1 mm in the S–I direction (Patient 2). For patients treated with IMRT, the average and maximum displacements were 1.9 and 5.1 mm in the A–P direction, 1.1 and 4.1 mm in the L–R direction, and 1.9 and 6.6 mm in the S–I direction.

DISCUSSION

The FE model and surface geometry maps with CT images were shown to be a useful tool to visualize the deformation of tumors during radiotherapy. Variations in the surface geometry map were also informative in indicating changes in tumor size, allowing the conclusion that surface geometry mapping can be a useful tool when comparing the effect of radiation among different tumor types, doses, and treatment types. It may be hypothesized that the surface geometry map may change unevenly if the distribution of cellular radiosensitivity, dose, or linear energy transfer, respectively, is heterogeneous in a tumor mass.

Table 3. Image correlation between surface geometry maps before and during treatment

	Correlation coefficient							
Patient	CT1	CT2	CT3	CT4	CT5	CT6	CT7	Average
1	0.927	0.856	0.642	0.777	0.760	0.817	0.787	0.795
2	0.841	0.717	0.678	0.678	0.682			0.719
3	0.887	0.882	0.729	0.797	0.739	0.824	0.810	0.810
4	0.916	0.904	0.923	0.807	0.720	0.734	0.792	0.828
5	0.922	0.851	0.941	0.917	0.931	0.931		0.915
6	0.874	0.839	0.703	0.729	0.804	0.771	0.767	0.784

Abbreviations: CT1 = CT images at 1 week; CT2 = CT images at 2 weeks, etc.

The 3D analysis of the target geometry using the surface geometry map showed that the six metastatic lymph nodes in this study shrank evenly, maintaining the original morphologic features throughout the treatment period. Image correlation analysis of the surface geometry maps showed that the maps obtained during treatment were strongly correlated with the initial map in all cases (overall average correlation coefficient, 0.808). The observation that tumors shrank uniformly throughout the treatment period was supported by quantitative analysis and by visual inspection. Uneven shrinkage of lymph nodes did not need to be considered in the radiotherapy of these patients. This means that changes in the 3D shapes of lymph nodes can be estimated by predicting the changes in volume, because the 3D shapes during the progress of the treatment can be obtained by shrinking the initial shape uniformly toward its center. This suggests that simulation methods that postulate even shrinkage of the tumor during radiotherapy can be applied as a tool to simplify the adaptive approach in IGRT. Elsewhere we have proposed the simulation method to predict changes in tumor volume during radiotherapy in cervical cancer (19). From those findings and also these, it is possible to postulate that the changes in the 3D shapes of lymph nodes during treatment—the deformation of metastatic lymph nodes—may be adjusted simply by interpolation or extrapolation from a comparison of CT images taken before and during radiotherapy.

Changes in target locations were almost all less than ±5 mm in the patients treated with IMRT; this is comparable to the setup errors in IMRT reported previously. Oita *et al.* analyzed the benefit of a real-time tumor-tracking radiotherapy setup in reducing setup errors (18). The results indicated that the range of displacement in a manual setup was about ±5 mm for the A–P, L–R, and S–I directions. In Patient 2, the change in target location reached nearly 10 mm. The reasons for the large change may have been related to the large size of the lymph nodes, patient immobilization, and the fusion process. This patient was immobilized using a thermoplastic mask without the three fiducial markers used in the other cases. The mask may not have completely prevented movement of the head and shoulders throughout the treatment. It is suggested that an accurate fusion process of the sequential images is essential to accurate analysis of the changes in the location of the tumor.

This study scanned patients with three fiducial markers. Because the markers are implanted into a rigid structure (mouthpiece), the position of each marker relative to the maxillary bone structure is stable, like a fixed marker to the bone, as also published previously (18). Each follow-up CT image

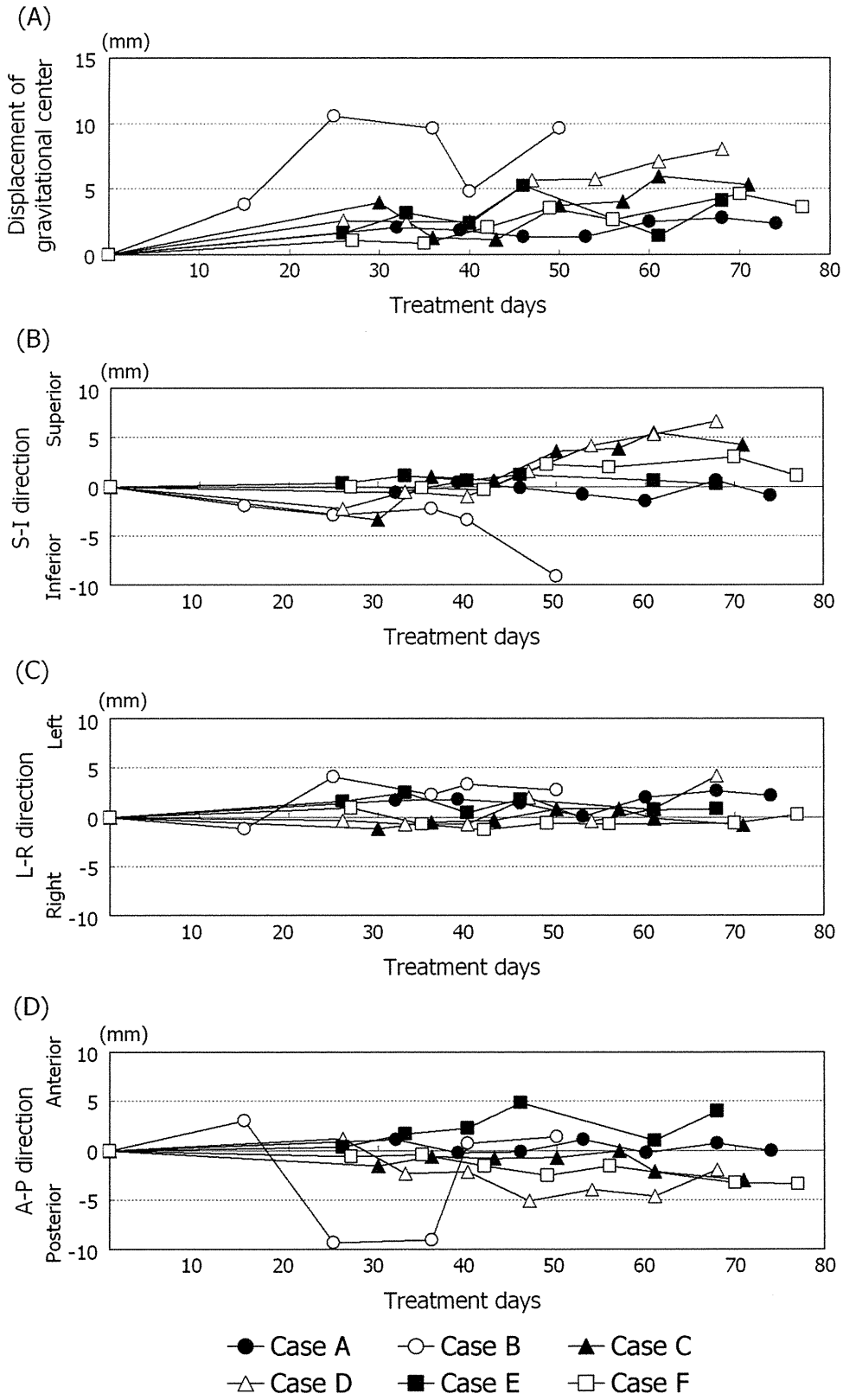

Fig. 4. Trajectories of the center of mass of the tumors during the course of treatment. (A) Overall displacement of the tumor. (B) Superior–inferior direction. (C) Left–right direction. (D) Anterior–posterior direction.

was shifted and rotated to fit the original CT image with reference to the location of these markers. By this process, the positions of the targets could be evaluated in the same coordinate system, without any effect by setup uncertainties. Thus, it was assumed that the effects of setup errors are negligible in this analysis and focus on the positional variations of the soft tissue caused by anatomic changes rather than setup errors. However, further study is required for a more

Table 4. Displacement of gravitational center of tumors in three directions during treatment

	A–P direction		L–R direction		S–I direction	
Patient	Average (mm)	Max (mm)	Average (mm)	Max (mm)	Average (mm)	Max (mm)
1	0.6	1.1	1.6	2.6	0.7	1.5
2	4.7	9.3	2.7	4.1	3.9	9.1
3	1.3	3.1	0.7	1.2	3.2	5.5
4	3.0	5.1	1.3	4.1	3.1	6.6
5	2.3	4.8	1.3	2.4	0.7	1.2
6	1.9	3.4	0.7	1.3	1.5	3.0
Total	2.2	9.3	1.3	4.1	2.2	9.1

Abbreviations: A–P = anterior–posterior; L–R = left–right; S–I = superior–inferior; Max = maximum.

accurate analysis to consider the possible bending of the cervical spine.

The CT scans for treatment planning are required to be acquired at a 2-mm slice width in our hospital. It would be advantageous to acquire all images with 2-mm thicknesses, but the weekly follow-up CT scans had to be made with a larger slice thickness because of limitations in imaging modalities. A slice thickness of the follow-up CT images during radiotherapy of 5 mm could lead to inaccuracies compared with 1- or 2-mm scans, especially in the S–I direction. By using a CT–CT fusion technique based on a mouthpiece with markers, the flexibility of the neck is not taken into account, and this flexibility influences the measurements of the location (center of gravity of the node).

CONCLUSION

The surface geometry map was useful in the accurate evaluation of the changes in volume and 3D shapes of the lymph nodes. The metastatic cervical lymph nodes in nasopharyngeal cancer patients were found to have decreased in size without significantly affecting the 3D morphologic features during radiotherapy. A surface geometry map based on the finite element model was shown to be useful in IGRT, particularly in the accurate recording and in the analysis of changes in tumor volumes and the 3D shape during radiotherapy.

REFERENCES

1. Barker JL Jr., Garden AS, Ang KK, *et al.* Quantification of volumetric and geometric changes occurring during fractionated radiotherapy for head-and-neck cancer using an integrated CT/Linear accelerator system. *Int J Radiat Oncol Biol Phys* 2004;59:960–970.
2. Li XA, Qi XS, Pitterle M, *et al.* Interfractional variations in patient setup and anatomic change assessed by daily computed tomography. *Int J Radiat Oncol Biol Phys* 2007;68:581–591.
3. Shirato H, Shimizu S, Kitamura K, *et al.* Organ motion in image-guided radiotherapy: Lessons from real-time tumor-tracking radiotherapy. *Int J Clin Oncol* 2007;12:8–16.
4. Riboldi M, Sharp GC, Baroni G, *et al.* Four-dimensional targeting error analysis in image-guided radiotherapy. *Phys Med Biol* 2009;54:5995–6008.
5. Den RB, Doemer A, Kubicek G, *et al.* Daily image guidance with cone-beam computed tomography for head-and-neck cancer intensity-modulated radiotherapy: A prospective study. *Int J Radiat Oncol Biol Phys 2009* 2010;76:1353–1359.
6. Wang J, Bai S, Chen N, *et al.* The clinical feasibility and effect of online cone beam computer tomography-guided intensity-modulated radiotherapy for nasopharyngeal cancer. *Radiother Oncol* 2009;90:221–227.
7. Houghton F, Benson RJ, Tudor GS, *et al.* An assessment of action levels in imaging strategies in head and neck cancer using TomoTherapy: Are our margins adequate in the absence of image guidance? *Clin Oncol* 2009;21:720–727.
8. Pawlowski JM, Yang ES, Malcolm AW, *et al.* Reduction of dose delivered to organs at risk in prostate cancer patients via image-guided radiation therapy. *Int J Radiat Oncol Biol Phys* 2010;76:924–934.
9. Varadhan R, Hui SK, Way S, *et al.* Assessing prostate, bladder and rectal doses during image guided radiation therapy: Need for plan adaptation? *J Appl Clin Med Phys* 2009;10:56–74.
10. Greene WH, Chelikani S, Purushothaman K, *et al.* Constrained non-rigid registration for use in image-guided adaptive radiotherapy. *Med Image Anal* 2009;13:809–817.
11. Hansen EK, Bucci MK, Quivey JM, *et al.* Repeat CT imaging and replanning during the course of IMRT for head-and-neck cancer. *Int J Radiat Oncol Biol Phys* 2006;64:355–362.
12. Smyth G, McCallum HM, Lambert EL, *et al.* A dose distribution overlay technique for image guidance during prostate radiotherapy. *Br J Radiol* 2008;81:890–896.
13. Ahunbay EE, Peng C, Godley A, *et al.* An on-line replanning method for head and neck adaptive radiotherapy. *Med Phys* 2009;36:4776–4790.
14. Wang H, Garden AS, Zhang L, *et al.* Performance evaluation of automatic anatomy segmentation algorithm on repeat or four-dimensional computed tomography images using deformable image registration method. *Int J Radiat Oncol Biol Phys* 2008;72:210–219.
15. Mohan R, Zhang X, Wang H, *et al.* Use of deformed intensity distributions for on-line modification of image-guided IMRT to account for interfractional anatomic changes. *Int J Radiat Oncol Biol Phys* 2005;61:1258–1266.
16. van Kranen S, van Beek S, Mencarelli A, *et al.* Correction strategies to manage deformations in head-and-neck radiotherapy. *Radiother Oncol* 2010;94:199–205.
17. Takao S, Tadano S, Taguchi H, *et al.* Analysis of three-dimensional characteristics in tumor morphology. *J Biomech Sci Eng* 2009;4:221–229.
18. Oita M, Ohmori K, Obinata K, *et al.* Uncertainty in treatment of head-and-neck tumors by use of intraoral mouthpiece and embedded fiducials. *Int J Radiat Oncol Biol Phys* 2006;64:1581–1588.
19. Takao S, Tadano S, Taguchi H, *et al.* Computer simulation of radiotherapy for malignant tumor: A mechanical analogy method. *J Biomech Sci Eng* 2009;4:576–588.

IOP PUBLISHING PHYSICS IN MEDICINE AND BIOLOGY

Phys. Med. Biol. **56** (2011) 965–977 doi:10.1088/0031-9155/56/4/006

A feasibility study of a molecular-based patient setup verification method using a parallel-plane PET system

Satoshi Yamaguchi[1], Masayori Ishikawa[1], Gerard Bengua[2], Kenneth Sutherland[1], Teiji Nishio[3], Satoshi Tanabe[1], Naoki Miyamoto[1], Ryusuke Suzuki[2] and Hiroki Shirato[4]

[1] Department of Medical Physics and Engineering, Hokkaido University Graduate School of Medicine, N-15 W-7 Kita-ku Sapporo 060-8638, Japan
[2] Department of Medical Physics, Hokkaido University Hospital, N-14 W-5 Kita-ku Sapporo 060-8648, Japan
[3] Particle Therapy Division, Research Center for Innovative Oncology, National Cancer Center, Kashiwa, 6-5-1 Kashiwano-ha, Kashiwa-shi, Chiba 277-8577, Japan
[4] Department of Radiology, Hokkaido University Graduate School of Medicine, N-15 W-7 Kita-ku Sapporo, 060-8638 Japan

E-mail: masayori@med.hokudai.ac.jp

Received 15 July 2010, in final form 9 December 2010
Published 19 January 2011
Online at stacks.iop.org/PMB/56/965

Abstract

A feasibility study of a novel PET-based molecular image guided radiation therapy (m-IGRT) system was conducted by comparing PET-based digitally reconstructed planar image (PDRI) registration with radiographic registration. We selected a pair of opposing parallel-plane PET systems for the practical implementation of this system. Planar images along the in-plane and cross-plane directions were reconstructed from the parallel-plane PET data. The in-plane and cross-plane FWHM of the profile of 2 mm diameter sources was approximately 1.8 and 8.1 mm, respectively. Therefore, only the reconstructed in-plane image from the parallel-plane PET data was used in the PDRI registration. In the image registration, five different sizes of ^{18}F cylindrical sources (diameter: 8, 12, 16, 24, 32 mm) were used to determine setup errors. The data acquisition times were 1, 3 and 5 min. Image registration was performed by five observers to determine the setup errors from PDRI registration and radiographic registration. The majority of the mean registration errors obtained from the PDRI registration were not significantly different from those obtained from the radiographic registration. Acquisition time did not appear to result in significant differences in the mean registration error. The mean registration error for the PDRI registration was found to be 0.93 $\pm$ 0.33 mm. This is not statistically different from the radiographic registration which had a mean registration error of 0.92 $\pm$ 0.27 mm. Our results suggest

that m-IGRT image registration using PET-based reconstructed planar images along the in-plane direction is feasible for clinical use if PDRI registration is performed at two orthogonal gantry angles.

(Some figures in this article are in colour only in the electronic version)

1. Introduction

Image guided radiotherapy (IGRT) techniques are presently used clinically to improve the accuracy of treatment delivery in photon radiation therapy. IGRT is used to correct for patient positioning errors prior to or during treatment by using image guided procedures. Patient setup can be verified through the co-registration of digitally reconstructed radiographs (DRR) and imaging plate (IP) or electronic portal imaging device (EPID) images taken using MV-x rays from a linear accelerator (Linac) while the patient is set up just prior to treatment (Dong and Boyer 1995, Gilhuijs *et al* 1996). Linac systems with on-board cone-beam computed tomography (CBCT) devices have also been developed (Pouliot *et al* 2005, Jaffray *et al* 2002, Groh *et al* 2002, Ford *et al* 2002, Munbodh *et al* 2006). CBCT allows the imaging of the target volume and organs at risk during treatment. Accuracy of patient setup verification error is important in order to ensure that the actual treatment geometry is as close as possible to the treatment planning geometry. At present, patient setup verification is done mostly by the alignment of bony structures in radiographic images taken during treatment and those used for treatment planning. The change in the tumor size and location inside the body is usually difficult to determine during treatment. Making the tumor visible in the irradiation field is thus desirable in order to improve setup verification accuracy.

Positron emission tomography (PET) based on sugar metabolism in the tumor caused by ^{18}F-fluorodeoxyglucose (FDG) uptake has been shown to be effective for distinguishing the tumor during diagnosis (Som *et al* 1980). Since PET images are functional images, they allow cell activity to be visible; thus, the tumor position can be determined. Another promising radioactive tracer for PET imaging is ^{18}F-fluoromisonidazole (FMISO) (Nehmeh *et al* 2008). FMISO is able to delineate hypoxic cells, which are known to be radiation resistant, in tumors. Clinical trials have demonstrated improved tumor control by delivering escalated doses to hypoxic tumor cells using IMRT and other techniques (Lee and Le 2008).

The spatial resolution and sensitivity of recent PET devices have also been significantly improved. This has been partly due to (1) the development of new detector elements such as BGO or GSO crystals, (2) the change in the acquisition method from 2D to 3D, and (3) the invention of depth-of-interaction (DOI) (Wienhard *et al* 2002, Yamaya *et al* 2003). The application of PET technology as a new modality for diagnostic procedures is also now being considered, for example, positron emission mammography (PEM) (Smith *et al* 2003, Huesman *et al* 2000, Zhang *et al* 2007, Raylman *et al* 2008, MacDonald *et al* 2009). In this study, we propose a PET-based molecular image guided radiation therapy (m-IGRT) system for patient setup verification in cases where significant tumor shrinkage or growth may occur, such as intracranial or head and neck. In the practical implementation of an m-IGRT system, it is preferable that the PET device is combined with a radiotherapy gantry to guarantee mechanical precision. There are, however, some restrictions on how the PET detectors can be mounted to the present gantry systems.

Because PET is a device that detects the annihilation radiation caused by positrons, it is necessary that at least a pair of opposed detectors are arranged to detect the two photons simultaneously. It is preferable that the isocenter of the pair of opposed detectors is identical to the isocenter of the radiotherapy unit. A structure with a wide open space between a pair of

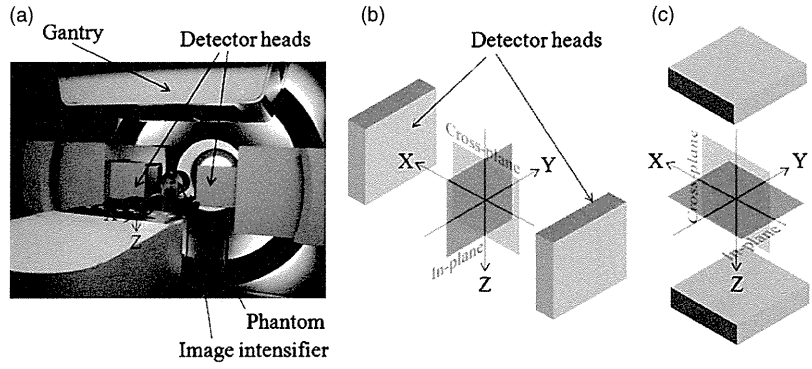

Figure 1. (a) The BOLPs with its gantry positioned at 0°. (b) The orientations of the in-plane and cross-plane directions in the BOLPs at a gantry angle of 0°. (c) The orientations of the in-plane and cross-plane directions in the BOLPs at a gantry angle of 90°.

opposed detectors is also needed so that the mega-voltage irradiation field does not become obstructed. The gantry rotation of the radiotherapy unit and the movement or the rotation of the couch must also be considered. Moreover, it is necessary to secure a wide field of view to use the device for setup verification. However, it is difficult in the conventional PET detector geometry, with ring-shape arrangement, to achieve this purpose. We therefore selected a geometry with a pair of opposing parallel-plane detectors. The advantage of this detector geometry is that it is structurally simple, and that it can be mounted easily on a radiotherapy gantry, similar to on-board imaging (OBI) devices.

In order to evaluate the feasibility of molecular image guided registration, we used the beam on-line PET system (BOLPs), developed at the Particle Therapy Division of the National Cancer Center, Kashiwa (Nishio *et al* 2005, 2006, 2010). The system consists of a pair of opposing parallel-plane detectors mounted on the gantry which can detect annihilation radiation produced by positron emitters (e.g. ^{15}O, ^{14}O, ^{13}N and ^{11}C). The BOLPs was originally developed for visualizing irradiation fields by measuring the activity of positron emitters which are generated by nuclear reactions from incident proton beams. The BOLPs has the same detector configuration as that of our proposed system.

In this paper, we report on the feasibility of a novel m-IGRT by comparing the PET-based digitally reconstructed planar image (PDRI) registration with radiographic registration.

2. Materials and method

2.1. Beam on-line PET system

The BOLPs at the National Cancer Center, Kashiwa, in Japan was used to verify the accuracy of patient setup verification in our proposed parallel-plane PET system. The BOLPs detector is mounted at the gantry of the proton irradiation system as shown in figure 1(a). The detector head consists of 3960 BGO crystals (2 mm × 2 mm × 20 mm) covering a 16 × 16 cm^2 field of view. The distance between the detector heads was fixed at 40 cm. Shown in figure 1(b) are the orientations of the in-plane and cross-plane directions for a gantry angle of 0°. The orientations of the in-plane and cross-plane directions for a gantry angle of 90° are illustrated in figure 1(c). The evaluation of the full width at half maximum (FWHM) of the profile of

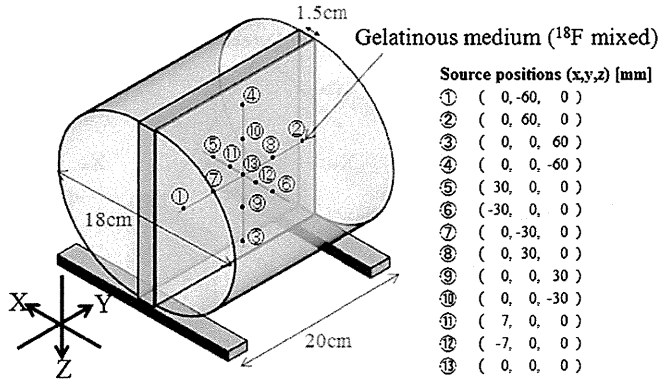

Figure 2. Cylindrical phantom with ^{18}F-sources placed in the positions as indicated.

2 mm diameter sources was done along the cross-plane and in-plane directions for a gantry angle of 0°. The FWHM of the profile is indicative of the spatial resolution.

In the image registration, only the reconstructed in-plane image from the parallel-plane PET data was used, and from here on, this in-plane image will be referred to as PDRI.

The BOLPs also includes an on-board x-ray system that allows the acquisition of radiographic images for patient setup verification. We compared the accuracy of radiographic and PDRI registrations.

2.2. *Image reconstruction method*

The detector configuration of the BOLPs is different from that of conventional PET systems in that they do not encircle the subject. Due to the parallel placement of the detector heads, there is limited angular sampling and loss of line of response (LOR) and the usual sinogram-based reconstruction method is not applicable. Therefore, the maximum likelihood-expectation maximization (MLEM) method (Shepp and Vardi 1982) was used in the LOR-based reconstruction using Siddon's algorithm (Siddon 1985).

In this study, only the detector sensitivity correction was applied while ignoring the other possible correction factors to account for scattering or absorption.

2.3. *Phantom configuration*

Two custom-made phantoms were used in our measurements. The first phantom was a polycarbonate cylindrical phantom with a width of 20 cm and a diameter of 18 cm. We refer to this phantom as the *cylindrical phantom*. It contained 13 cylindrical radiation sources (each with a diameter of 2 mm and width of 2 mm) that were arranged as shown in figure 2. The other phantom was a polycarbonate plate containing five cylindrical radiation sources of various diameters (i.e. 8, 12, 16, 24, 32 mm) with 1.5 cm width, representing different tumor sizes as shown in figure 3(a). This was attached to an acrylic slab (height: 20 cm, width: 18.5 cm, depth: 0.3 cm) as shown in figure 3(b). In this paper, we refer to this phantom setup as the *tumor phantom*. The radiation sources in both the cylindrical phantom and the tumor phantom used ^{18}F that was homogeneously mixed in a gelatinous medium.

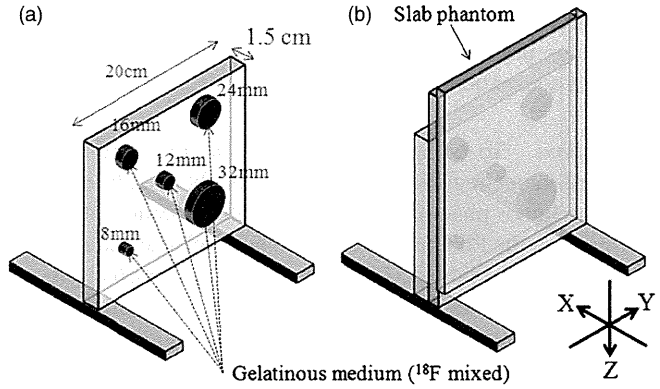

Figure 3. (a) Polycarbonate plate containing ^{18}F-sources of various diameters representing different tumor sizes. (b) The plate in (a) attached to an acrylic slab phantom.

2.4. FWHM of the profile of 2 mm diameter sources

The unique detector geometry of the BOLPs does not allow the use of the filtered back projection reconstruction as specified in the National Electrical Manufactures Association (NEMA) standard which is used for the evaluation of PET detectors. Therefore we used a modified method for image reconstruction based on PEM (Smith *et al* 2004, MacDonald *et al* 2009), which has a detector geometry similar to the BOLPs. PEM devices and the BOLPs have anisotropic spatial resolutions because the detectors do not encircle the object and do not rotate to acquire the full 360° angular sampling required for full three-dimensional tomography. Parallax error caused by the thickness of scintillation crystals is considered (Hoffman *et al* 1989, Lerche *et al* 2005).

We evaluated the FWHM of the profile of 13 cylindrical sources with a diameter of 2 mm and width of 2 mm using the cylindrical phantom shown in figure 2. The ^{18}F activity was 40 kBq ml^{-1}. The projection data were measured for 15 min at a gantry angle of 0°. The image reconstruction via the MLEM method was applied with the pixel size and slice thickness of 1.00 mm and a reconstruction volume of 15 × 15 × 15 cm^3.

2.5. Registration experiments

2.5.1. PDRI registration. PDRI registration was performed by comparing the in-plane digitally reconstructed planar image from the BOLPs and the image obtained from a conventional PET (Discovery ST, General Electric, Schenectady, New York). The pixel size and slice thickness were 3.91 and 3.27 mm, respectively. We placed the tumor phantom in a conventional PET such that the polycarbonate plate was parallel to the longitudinal axis and the center of the plate aligned with the isocenter. Data collection was performed for 15 min.

The tumor phantom was then placed at the isocenter of the BOLPs to obtain the data for the PDRI. Data were also collected for two additional conditions where the tumor phantom was displaced by 2 and 7 mm along the *Y*-axis, away from the isocenter to avoid the observer's bias from trial learning. Each measurement with the BOLPs was carried out for 5 min. The activity of ^{18}F was 20 kBq ml^{-1} and the background activity was 4 kBq ml^{-1}. The gantry angle was fixed at 0°. MLEM image reconstruction was applied with the pixel size and slice thickness of 1.00 mm and a reconstruction volume of 15 × 15 × 5 cm^3. PDRIs corresponding

to 1, 3 and 5 min measurements were generated for each setup position. Image registration based on the PDRI for each setup position was performed by five observers. The reference image was reconstructed from a conventional PET image.

2.5.2. Radiographic registration. To compare the accuracy of radiographic and PDRI registrations, we also performed image registration using images obtained from an x-ray CT and a fluoroscopic system. The tumor phantom was placed at the isocenter of the x-ray CT following the same setup as used in the PET measurement. The pixel size and slice thickness were 0.98 and 1.25 mm, respectively. Fluoroscope images of the tumor phantom were also taken using the installed fluoroscopic system in the proton irradiation system. The position of the tumor phantom was subsequently moved along the *Y*-axis to take additional data at 2 and 7 mm from the isocenter. The reference image used in the radiographic registration was the DRR reconstructed from x-ray CT.

2.5.3. Registration accuracy evaluation. To evaluate the accuracy of the registration methods, image registration trials using in-house software were performed for ten trials. Each trial consisted of five different images shown twice to the observers. Five observers estimated the shifts in each trial. From the image registration data, we calculated the registration error (RE) using equation (1). Actual shift (Y_{actual}) was 0, 2 and 7 mm along the *Y*-axis. Z_{obs} and Y_{obs} in the equation refer to the observed translation along the *Z*-axis and *Y*-axis respectively performed by the five subjects. Statistical analysis was performed based on the registration error for both the radiographic and PDRI registrations:

$$\text{RE(mm)} = \sqrt{(Z_{\text{obs}})^2 + (Y_{\text{obs}} - Y_{\text{actual}})^2}. \tag{1}$$

Here RE denotes the registration error, Z_{obs} the observed translation along the *Z*-axis, Y_{obs} the observed translation along the *Y*-axis and Y_{actual} the actual setup couch translation along the *Y*-axis (0, 2, 7 mm).

2.5.4. Statistical analysis. Statistical analysis of our data was performed using JMP 8 (SAS Institute Inc.) software. The mean registration error and standard deviation (SD) for the various diameters were determined based on the acquisition time for data collection (i.e. 1, 3 and 5 min) and modality (BOLPs, x-ray fluoroscopy). Data were analyzed by one-way ANOVA, while the differences among means were analyzed by two-sided Student's *t*-test with the level of statistical significance set to $p < 0.05$.

3. Results

3.1. FWHM of the profile of 2 mm diameter sources

Figure 4 shows the reconstructed in-plane and cross-plane images of the cylindrical phantom corresponding to a gantry angle of 0°. The reconstructed source diameter at the central position was larger than the others due to blurring caused by adjacent sources. The FWHM of each radiation source is shown in figure 5. The mean ± SD for FWHM was 1.8 ± 0.3 mm in the in-plane image and 8.1 ± 1.2 mm in the cross-plane image at a gantry angle of 0°.

3.2. Registration accuracy evaluation

Shown in figure 6 are the PDRIs of the tumor phantom at a gantry angle of 0°. Images from left to right correspond to the three acquisition times (1, 3 and 5 min) for data collection,

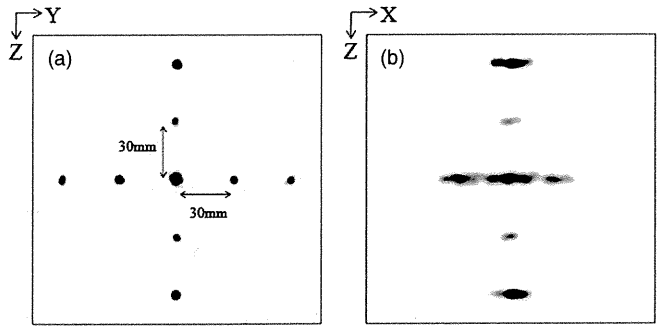

Figure 4. Planar images of the ^{18}F-sources along the (a) in-plane and (b) cross-plane directions reconstructed from the BOLPs data at a gantry angle of 0°.

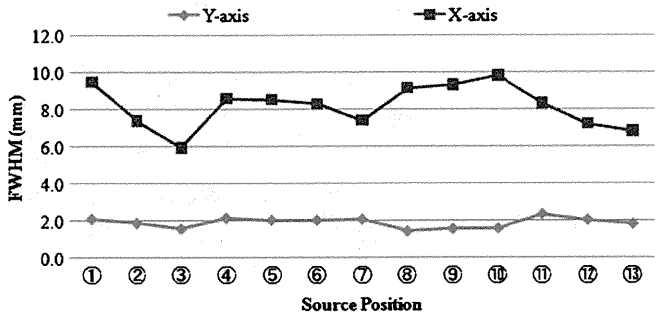

Figure 5. FWHM of the profile of the 2 mm diameter sources in the cylindrical phantom of figure 2.

while those from top to bottom correspond to the positions of the phantom (0, 2 and 7 mm) during data acquisition. The gray-scale window level of the images was adjusted to enhance the contrast. The measured activity at the source increased linearly as a function of acquisition time, and contrast to the background was constant and no inconsistency was observed among the three positions.

Figure 7 shows the variations in the observed PDRI and radiographic registration errors with respect to the acquisition time, phantom position and source diameter. PDRI registration errors were obtained from the registration of the reconstructed PET and BOLPs planar images. The radiographic registration errors were obtained from registration of DRR and portal (x-ray) images. The dependence of the registration error on the phantom position was not seen for each diameter.

Shown in table 1 are the mean ± SD of the registration errors based on our ANOVA. For the diameter of 8 mm the mean registration error of the PDRI registration appears to be influenced by the acquisition time with the longest acquisition time having the least mean registration error. The registration error for the radiographic registration was comparable to that of the shortest acquisition time of 1 min for the PDRI. The differences in the registration error between the image registration modalities listed in table 1 for the 8 mm diameter were found to be significant at a p-value of <0.0001. On the other hand, the mean registration error in all four registration methods for the diameter of 12 mm was found to be statistically insignificant ($p = 0.3545$) with their mean registration error ranging between 0.49 and 0.63. For diameters of 16 and 24 mm, the three acquisition times using the PDRI resulted in similar

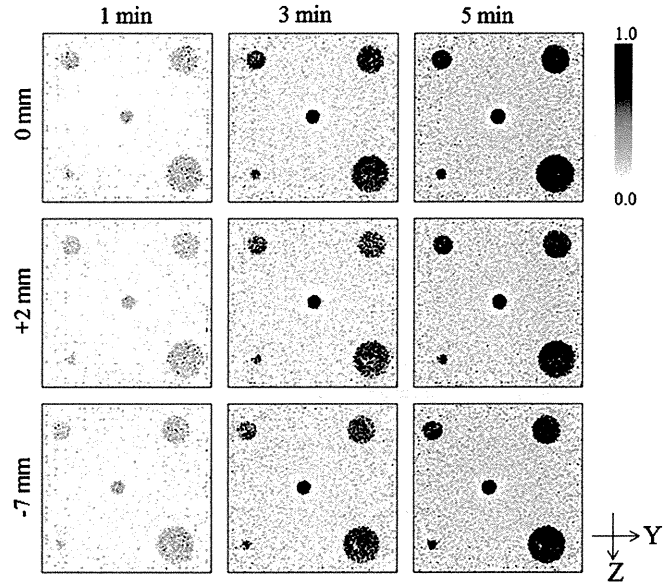

Figure 6. Planar image reconstructions of the ^{18}F-sources in the tumor phantom of figure 3(b). Shown are the results for three phantom positions relative to the isocenter and at the acquisition times of 1 , 3 and 5 min, respectively.

Table 1. Statistical comparison of registration errors from PDRI and radiographic registrations using ANOVA. PDRI registration was performed using reconstructed planar images from PET data (at the acquisition time of 15 min) and BOLPs data (at the acquisition times of 1, 3 and 5 min). Radiographic registration was performed using DRR and portal (x-ray) images.

	Diameter				
Registration method	8 mm	12 mm	16 mm	25 mm	32 mm
PDRI (1 min)	1.07 ± 0.42	0.49 ± 0.34	1.02 ± 0.44	1.28 ± 0.35	1.12 ± 0.39
PDRI (3 min)	0.87 ± 0.29	0.59 ± 0.24	1.01 ± 0.38	1.25 ± 0.29	0.86 ± 0.37
PDRI (5 min)	0.56 ± 0.26	0.60 ± 0.24	1.00 ± 0.34	1.30 ± 0.26	0.88 ± 0.32
Radiographic (x-ray)	0.98 ± 0.28	0.63 ± 0.30	0.87 ± 0.31	0.95 ± 0.20	1.17 ± 0.26
p-value	<0.0001*	0.3545	0.522	0.0003*	0.0044*

*Significant ($p < 0.05$).

registration errors and a relatively smaller registration error for the radiographic registration. However, the difference between the PDRI and radiographic registrations was found to be statistically significant only for 24 mm at $p = 0.0003$. A significant difference between the PDRI and radiographic registration errors was obtained for the 32 mm diameter.

The statistical comparisons of the mean registration error and SD for each source diameter obtained from the PDRI registration at 1, 3, and 5 min and the radiographic registration are shown in figures 8 and 9.

For the diameter of 8 mm, the differences in the registration error for the three acquisition times used in the PDRI registration were found to be statistically significant. However, when compared to the registration error of the radiographic registration, only the 5 min PDRI data yielded a significant difference. The mean registration errors for the image registration

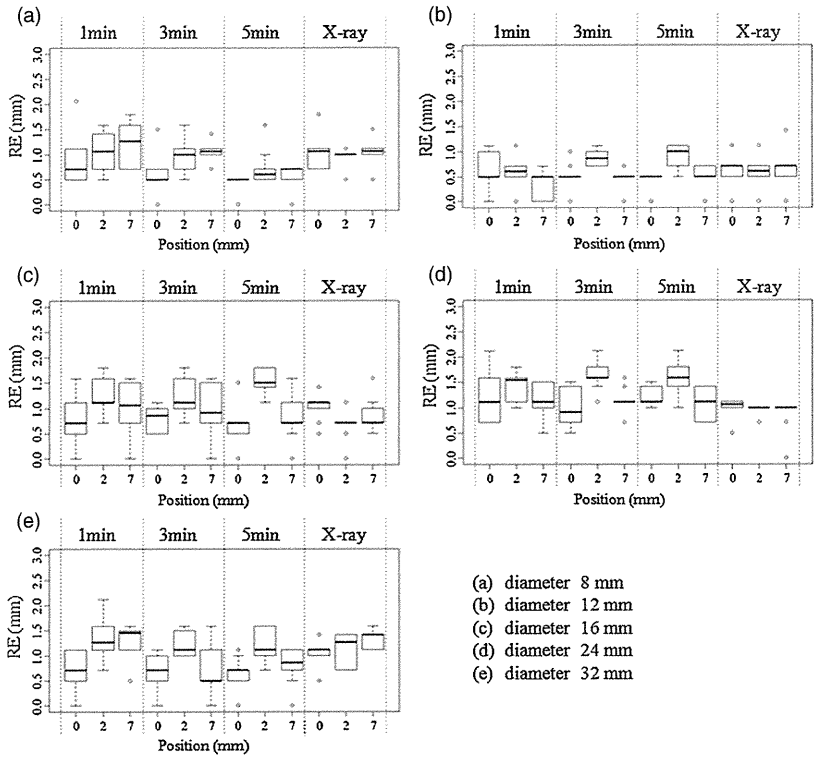

Figure 7. Registration errors for the tumor phantom of figure 3(b). Shown are the results for three phantom positions relative to the isocenter (0), isocenter + 2 mm (2) and isocenter + 7 mm (7) at the acquisition times of 1 , 3 and 5 min, respectively.

conditions shown in figures 8(b) and (c) for diameters of 12 and 16 mm were not statistically different. However, a larger variation in the computed registration error was observed for 16 mm.

For the diameter of 24 mm, the mean registration error obtained for the radiographic registration was found to be significantly smaller compared to those obtained using the PDRI registration method. Furthermore, the acquisition time did not appear to result in significant differences in the mean registration error for the PDRI registration. Like those of the results for the 8 mm diameter, the mean registration error for the 32 mm diameter decreased with the acquisition time in the PDRI registration.

A comparison of the registration error SDs is shown in figure 9 for the various diameters and data acquisition methods. The SDs for most of the results were not statistically different. The image registration SDs of the PDRI at 3 min acquisition time were statistically the same as those of the radiographic registration.

4. Discussion

An overall evaluation of the accuracy of PDRI registration independent of the source size is necessary. We therefore performed a comparative study of the registration error obtained with PDRI and radiographic registrations for a number of hypothetical source sizes. The cumulative

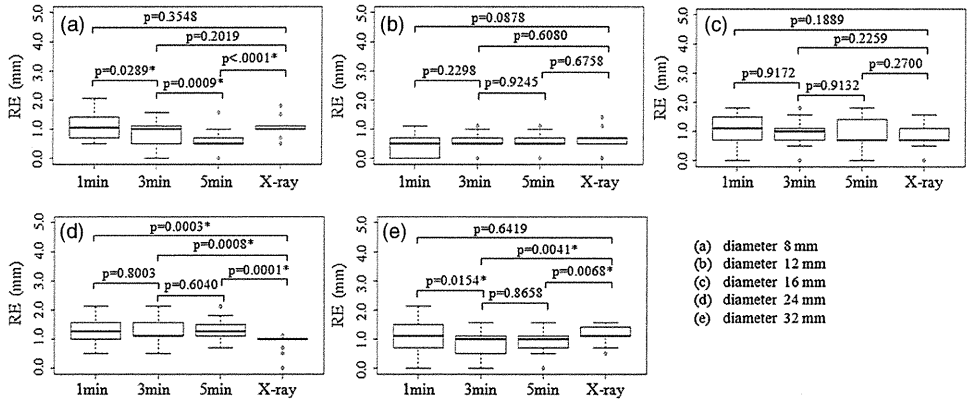

Figure 8. Statistical comparison of the mean registration error for the five cylindrical sources with diameters of 8, 12, 16, 24 and 32 mm using Student's t-test at $p < 0.05$ significance level.

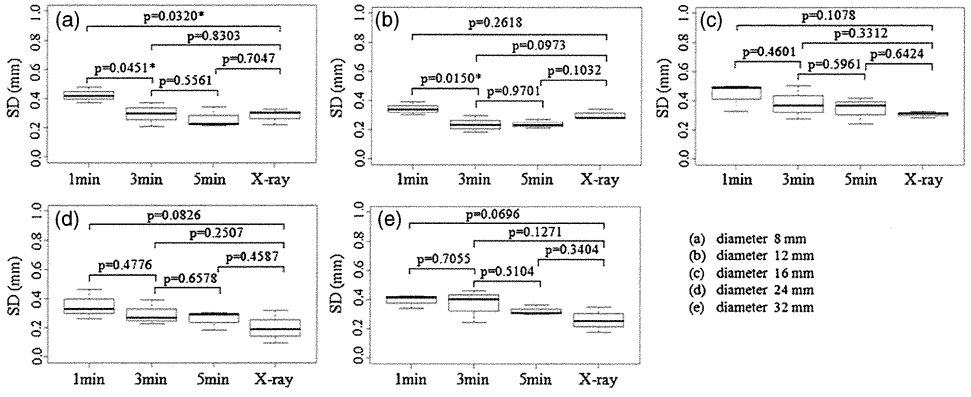

Figure 9. Statistical comparison of the standard deviation of the mean registration error for the five cylindrical sources with diameters of 8, 12, 16, 24 and 32 mm using Student's t-test at $p < 0.05$ significance level.

mean registration error and SD for five different source sizes using four registration conditions (i.e. PDRI at 1, 3 and 5 min acquisition times and radiographic registration) are shown in figure 10. A general trend of decreasing mean registration error and SD for longer acquisition time is seen for the PDRI registration. The 3 min data acquisition in the BOLPs yielded comparable results to radiographic registration, while the 5 min acquisition appears to result in lower registration error.

Our tumor phantom experiments show that the mean of the registration errors for the PDRI is approximately 0.93 mm and the SD is approximately 0.33 mm. This is not statistically different from the radiographic registration which had a mean registration error of 0.92 $\pm$ 0.27 mm.

Although there are no reports on the accuracy of image registration using molecular imaging, there have been a number of publications regarding the accuracy of DRR and EPID image registration. Dong and Boyer (1995) showed that in their phantom image registration study, the correlation procedure had a SD of 0.5 mm in aligning translational shifts. Gilhuijs

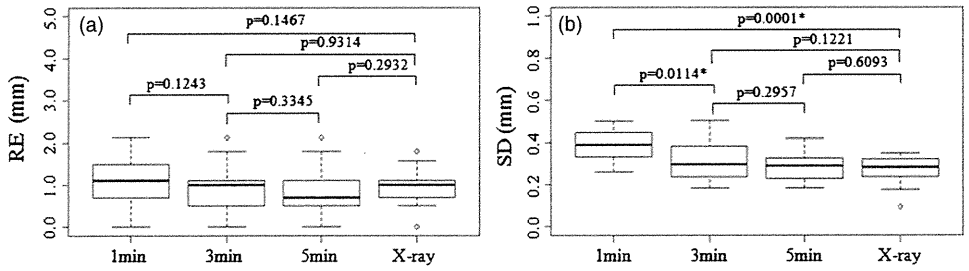

Figure 10. Statistical comparison of (a) the mean registration error and (b) the standard deviation for an overall evaluation using Student's t-test at $p < 0.05$ significance level.

et al (1996) registered 2D portal images with CT data, and their automatic 3D analysis of patient setup accuracy was found to be accurate to within 1 mm in the translational directions. In the clinical evaluation of patient setup errors using portal imaging by Hurkmans *et al* (2001), it was reported that setup errors were less than 2.0 mm (1SD) for head and neck, 2.5 mm (1 SD) for prostate, 3.0 mm (1 SD) for general pelvic and 3.5 mm (1 SD) for lung cancer. The study also noted that the setup verification accuracy varies widely, depending on the treatment site, method of immobilization and institution.

The registration error for the PDRI was lower than that of previously reported radiographic registrations. This could be due to the fact that the image registration was performed with ^{18}F-source itself, not with the skeletal structure, or that there was a phantom dependence. Nevertheless, the registration error for PDRI registration was not significantly different from that of radiographic registration in our experiments. As shown in figure 10(b), the registration error is dependent on the data acquisition time. In order to apply PDRI registration clinically, the acquisition time should be taken into account. A longer acquisition time will result in lower registration error, but it will cause patient discomfort. An optimum acquisition time needs to be considered while maintaining the registration accuracy. However, this is complicated because it depends on the tumor and normal tissue uptake and radiation attenuation in the patient's body. Patient immobilization may also be necessary in order to minimize the effects of inter- and intra-fraction motion caused by patient movement. The effect of respiratory induced motion should be considered in future works.

If FDG is used as the tracer in PDRI registration, it will also be taken up in normal organs such as the brain, liver, kidneys, bladder, etc. This will be a problem in this image registration modality. However, because of the high spatial resolution of our parallel-plane PET system along the in-plane direction, it should be possible to distinguish the tumor FDG uptake from that of the adjacent normal organs which also accumulate FDG. As shown in Figure 4, at the same gantry angle, the corresponding cross-plane image has a much lower resolution and therefore would not be usable for image registration.

Conventional radiographic registration is performed by taking a portal planar image in the LR direction with the gantry at 0° and afterward rotating the gantry to 90° in order to take another portal planar image at the AP direction. These left–right (LR) and anterior–posterior (AP) images are separately registered with corresponding DRR images to complete the radiographic registration process. In our m-IGRT system, the same setup verification procedure using LR and AP images taken separately at different gantry angles will have to be performed. In this case, the PDRI for the LR direction will be the reconstructed in-plane image from the parallel-plane PET data obtained at a gantry angle of 0°. On the other hand, the PDRI for the AP direction will be the reconstructed in-plane image from parallel-plane